Stochastic finite element analysis of the diametral compression test of powder compacts and porous materials

Jose Andres Alvarado-Contreras (ajose.ula@gmail.com)
University of the Andes - La Hechicera Campus https://orcid.org/0000-0001-5663-1192
Alexis Andres Lopez-Inojosa
ULA: Universidad de Los Andes

Research Article

Keywords: Powder compacts, porous materials, splitting tensile test, experimental test assessment, uncertainty propagation

Posted Date: April 29th, 2021

DOI: https://doi.org/10.21203/rs.3.rs-310102/v1

Stochastic finite element analysis of the diametral compression test of powder compacts and porous materials

J.A. Alvarado-Contreras[1,*] and A.A. López-Inojosa[2]

[1]School of Mechanical Engineering, University of the Andes, Mérida 5101, Venezuela
ORCID 0000-0001-5663-1192

[2]School of Civil Engineering, University of the Andes, Mérida 5101, Venezuela
ORCID 0000-0002-9758-9661

[*]Address correspondence to
Universidad de Los Andes, Núcleo "Pedro Rincón Gutiérrez" - Sector La Hechicera,
Facultad de Ingeniería, Escuela de Ingeniería Mecánica, Mérida 5101, Mérida, Venezuela
ajose.ula@gmail.com
+58 424 7795359

Stochastic finite element analysis of the diametral compression test of powder compacts and porous materials

Abstract

This paper presents a stochastic finite element approach for modeling the mechanical behavior of powder compacts and porous materials under diametral compression test conditions. The main goal is assessing the validity of the diametral compression test as an indirect technique to estimate tensile strengths of brittle or quasi-brittle materials exhibiting porosity heterogeneity. Thus, the study seeks to predict the influence of porosity randomness on stress distributions and the spatial location of the highest tensile stress on thin disc-shaped specimens. The proposed formulation uses a stochastic framework that couples a random spatial field to the finite element analysis to include non-deterministic features. Two case studies consider comparable targets for the mean porosity but different coefficients of variations. For each case study, a total of 1000 realizations are conducted under identical loading and boundary conditions. The predicted stress distributions are compared to the ones from homogenous closed-form solutions from the literature. Then, the expected magnitude and location of the maximum tensile stress are evaluated by statistical means. Findings from the stochastic model show that porosity randomness induces stress concentration around less dense volumes and location deviation of the maximum tensile stress from the center of the discs. Likewise, porosity heterogeneity could affect the accuracy of experimental diametral compression tests even for small variance cases; and so, the reliability of the mechanical properties derived from models based exclusively on the classic assumption of material homogeneity.

Keywords – Powder compacts; porous materials; splitting tensile test; experimental test assessment; uncertainty propagation

1. INTRODUCTION

Porous materials have found ordinary and extensive uses in diverse fields. From biomedical to aerospace applications, porous materials prove successful when biomimetic properties are of particular importance or when high mechanical strengths are required with simultaneous weight reduction [1–3]. Porous surfaces ensure a proper bond between the prosthesis and the host bone in implants made of biocompatible materials such as calcium phosphate ceramics [4–6]. Porous materials have also found widespread uses in the aerospace industry, going from simple filtration systems to applications such as gas sensors and separators, thermal isolators, or heat exchangers [7–9]. For this reason, a precise mechanical characterization of porous materials is of significance to ensure the highest possible performance of the intended engineering application.

Porous materials are naturally found or industrially produced by partially densifying powder mixes using compaction techniques [10]. Properties of porous materials are not only influenced by the compaction pressures and temperatures but also by the physicochemical properties of the raw powders [11]. Among other features, particle size, particle shape, particle size distribution, roughness, and surface impurities govern the kinetics of consolidation of powder materials and so final mechanical properties. For instance, powders with low flowability and strongly agglomerated can lead to materials with broad pore size distributions or even multimodal distributions [12].

Compressive and tensile strengths, stiffness, and fracture toughness are among the most important parameters to characterize porous materials [13]. Thus, different experimental approaches are available to assess these properties. In recent decades, the diametral compression test has become an accepted experimental technique to gauge indirectly tensile strengths of brittle or quasi-brittle materials. The diametral compression test, *a.k.a*. Brazilian test, was initially designed to estimate tensile strengths of concretes [14]. Like the experimental setups schemed in Fig. 1, the Brazilian test consists of a disc-shaped specimen subjected to diametral forces applied by two flat plates or curved jaws. [15]. In a thin disc, loading conditions induce a plane stress state with nearly constant tensile stress along the loaded diameter and compressive stress along with the perpendicular one.

Numerous studies are available on the Brazilian test to evaluate properties of rocks [16] along with the ones of other homogeneous and heterogeneous media [17–22]. Among those works, different modeling approaches have been successfully implemented in commercial or in-house finite element codes; however, to the best authors' knowledge, none of them has considered modeling diametral compression of powder compacts from a stochastic viewpoint.

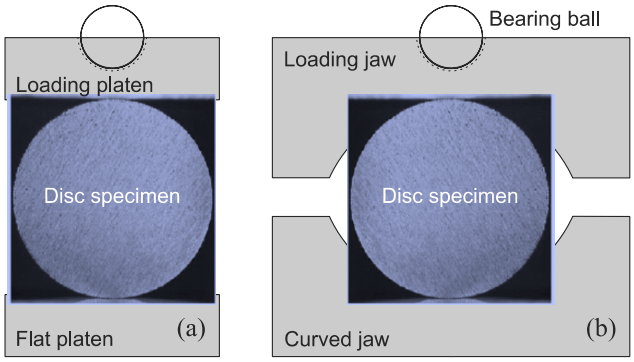

Fig. 1 Experimental setups using (a) standard flat loading platens and (b) curved loading jaws

Always there has been an accumulating interest in the Brazilian test to assess the tensile strengths of diverse heterogeneous materials. For instance, Yue et al. [23] used digital image techniques to carry out finite element simulations of non-homogeneous geomaterials under diametral compression test conditions, finding that stress distributions and initial crack location are significantly affected by the internal structure of those materials. Jonsén et al. [24] employed a Brazilian test setup to study the mechanical strength, fracture instability onset, and fracture energy of green iron powder compacts of different densities. They suggested a procedure to estimate tensile strengths by analyzing the linear to non-linear transition from load-displacement curves. From the experimental outcomes, Jonsén et al. [24] discussed the large spread observed in the correlation between green strengths and densities. Jonsén and Haggblad [25] studied the tensile fracture of metal powder compacts by considering a constitutive model formulated in terms of non-linear fracture mechanics and coupled to a perfect plastic failure envelope with a hardening cap. Then, Korachkin et al. [26]

employed an experimental diametral compressive setup to assess elastic moduli and tensile strengths of alumina and Distaloy AE compacts. They compared the attained resistances and failure modes to the ones obtained from three-point bending tests, suggesting that result differences are because heterogeneity introduces local weaknesses that prompt failure. Seeber et al. [27] investigated the suitability of the Brazilian test alongside the 3-point bending and compression tests as characterization techniques of the mechanical response of highly porous alumina with diverse microstructures. Cui et al. [28] presented a micromechanical model to predict properties of brittle materials with different porosities and pore sizes in diametral compression. In that work, they evaluated the microscale mechanical properties and correlated the impact of porosity and pore size on the fracture strength, Weibull modulus, and degradation processes of the specimens.

Uncertainties in powder material design are unavoidable. Parameters such as powder mix properties or compaction processes involve significant levels of uncertainty. Consequently, some numerical simulations are non-representative studies when based exclusively on averaged properties and limit isolated phenomena. Thus, this paper presents a computational approach in the behavior of disc-shaped specimens of porous materials in diametral compression to gain insight into inhomogeneity's significance on test results. The parameter of interest is porosity, which defines the pore volume to total volume fraction. In a probabilistic framework, a spatial stochastic field describes material heterogeneity, and a finite element model estimates displacement and stress fields. The spatial random field employs a discretization method that guarantees a truthful representation of the material together with a computational cost reduction.

The paper organizes as follows. The "Materials and methods" section highlights the most relevant equations of the proposed model. First, the constitutive formulation is presented along with an introduction to the approach used to approximate porosity random fields. Next, the finite element stiffness matrix is expressed in terms of the uncertain parameter. In the last part of the paper, the "Numerical example and discussion" section presents two case studies and how the model is used to simulate the mechanical behavior of disc-shaped specimens with non-homogeneous porosity distributions. Results are compared

with the ones obtained from analytical and numerical models under the assumption of material homogeneity, and finally, conclusions are drawn.

2. MATERIALS AND METHODS

This section deals with the procedures that translate the material behavior into the form of constitutive relationships and mathematical terms. In particular, attention is on the modeling strategy of porous disc-shaped specimens in diametral compression and on the uncertainty propagation through the outcomes. Considering porosity as a time-independent parameter, it turns out that pore collapse does not affect deformations and that the deformation history does not govern stress states. Consequently, the material behaves as isotropic linear elastic with no local viscous-plastic effects. Thus, only two independent elastic properties: the elastic modulus and Poisson's ratio, describe the linear behavior. In the formulation, the material is thought of being a porous skeleton containing open and closed pores, which distribute randomly in shape and size. Likewise, the total material volume is the volume sum of substance and pores. Thus, using continuum mechanics, the so-called effective local elastic modulus is porosity-dependent [29, 30]. In contrast, Poisson's ratio is an intrinsic property that does not vary significantly within the mesoscale.

2.1. Constitutive formulation

The properties of non-homogeneous materials depend on the links between the different length scales and the complexity of each substructure [31–33]. For instance, heterogeneities induce randomness and affect both the local and the overall mechanical behavior of materials. However, to cast the problem on a single scale, the current formulation does not involve all small-scale features on the macroscopic response. Hence, field equations describing the elastic behavior are based upon continuum mechanics and given by the motion equation, the kinematic relationships, and the constitutive law. For the case studies, specimens are subjected to in-plane loads, and the thickness is considered much smaller than the diameter, as illustrated in Fig. 2a. In such circumstances, it is quite convenient to treat the problem as

a plane stress case defined on the domain D with boundaries $\partial\mathsf{D}$, as shown in Fig. 2b. Accordingly, (*i*) the $xy-$plane coincides with the middle plane of the disc, (*ii*) the contact between the disc and the loading jaw induces load distributions, and (*iii*) all $z-$stress components vanish. The residual boundaries $\partial\mathsf{D}\setminus\partial\mathsf{D}_u$ are stress-free.

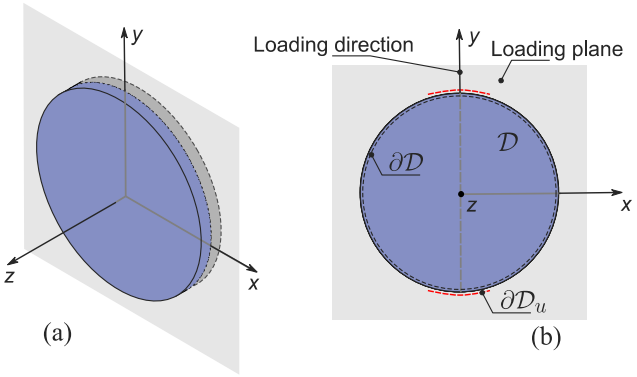

Fig. 2 (a) Three-dimensional specimen domain and
(b) two-dimensional modeling domain

Thus, from the above hypotheses, the functional relationship between stress σ and strain ε components for isotropic materials is given as

$$\begin{Bmatrix} \varepsilon_x \\ \varepsilon_y \\ 2\varepsilon_{xy} \end{Bmatrix} = \frac{1}{E}\begin{bmatrix} 1 & -\nu & 0 \\ -\nu & 1 & 0 \\ 0 & 0 & 2(1+\nu) \end{bmatrix}\begin{Bmatrix} \sigma_x \\ \sigma_y \\ \sigma_{xy} \end{Bmatrix} \tag{1}$$

where E and ν are respectively the elastic modulus and Poisson's ratio. The out-of-plane strain component is written as $\varepsilon_z = -\nu/(1+\nu)(\varepsilon_x + \varepsilon_y)$.

Material heterogeneities introduce local weaknesses that trigger stress concentrations and strength drops. As pointed out, the material is non-homogeneous due to the inherent porosity variability. Thus, the constitutive model captures the underlying variation via a spatial random field function. This function contains essential local information from the mesoscale and provides a realistic approximation of the material through the effective property. Therefore, upscale simulations are performed, introducing the material stiffness as

a spatial field and assuming a deterministic relationship between porosity and elastic modulus.

2.2. Description of the random porosity field

In this work, porosity variability is described by using spatial statistics, where the local quantity is defined by a probability distribution and correlated with values at adjacent locations. Thus, let $\boldsymbol{x}$ be a material point within a circular domain $\{\boldsymbol{x} \mid x^2 + y^2 \leq R^2\}$, where R is the specimen's radius. Then, let us define $\Theta(\boldsymbol{x})$ as a real-valued random function representing porosity at each point. From the theory of probabilities [34], $(\Omega, \mathsf{F}, \mathsf{P})$ represents the probability space components, *i.e.*, the outcome sample space Ω, the event collection F over the subsets of Ω, and the probability measure P of each member of F. Thus, let us think of the random spatial field as a mapping defined from the product space $\mathsf{R}^2 \times \Omega$,

$$\Theta(\boldsymbol{x}, \omega) : \mathsf{R}^2 \times \Omega \longrightarrow \mathsf{R} \tag{2}$$

where ω is a realization sampled from the probability space Ω according to P. Realizations are independent of each other and equally likely. Figure 3 depicts the proposed probability space with a selection of porosity realizations. Accordingly, $\Theta(\bullet, \omega)$ refers to the random variable resulting from realization ω, while $\Theta(\boldsymbol{x}, \bullet)$ represents the random variable for a fixed $\boldsymbol{x}$.

Material variability can be quantified by a probability distribution when sufficient statistical information is available. In what follows, let us suppose that the probability measure is known and that statistical parameters are estimated. In the case of random fields, the classic definition of mean and variance can be extended directly [35]; therefore, the expected value for $\Theta(\boldsymbol{x}, \bullet)$ is given as

$$\overline{\Theta}(\boldsymbol{x}) = \mathsf{E}[\Theta(\boldsymbol{x}, \bullet)] \tag{3}$$

and the deviation from this expected value, i.e., the variance, as

$$\mathrm{var}[\Theta(\boldsymbol{x}, \bullet)] = \mathsf{E}[\Theta(\boldsymbol{x}, \bullet) - \overline{\Theta}(\boldsymbol{x})]^2 \tag{4}$$

where $\mathsf{E}[\bullet]$ is the mathematical expectation operator.

Likewise, for each $(\boldsymbol{x}, \boldsymbol{x}')$, the covariance function is expressed as

$$\operatorname{cov}[\Theta(\boldsymbol{x}, \bullet), \Theta(\boldsymbol{x}', \bullet)] = \mathsf{E}\left\{[\Theta(\boldsymbol{x}, \bullet) - \overline{\Theta}(\boldsymbol{x})][\Theta(\boldsymbol{x}', \bullet) - \overline{\Theta}(\boldsymbol{x}')]\right\} \tag{5}$$

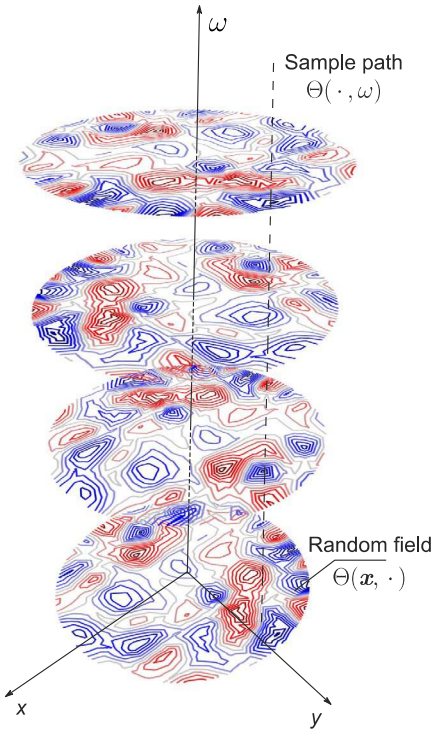

Fig. 3 A selection of realizations in the porosity space

For the case that concerns us, porosity sample fields are regarded as uncorrelated random variables with zero mean and finite variance, arranged along with a spatial space in R^2; *i.e.*,

$$\mathsf{E}[\Theta(\boldsymbol{x}, \bullet)] = 0 \text{ for all } \boldsymbol{x}, \text{ and } \boldsymbol{K}(\boldsymbol{x}, \boldsymbol{x}', \bullet) = \mathsf{E}\left\{[\Theta(\boldsymbol{x}, \bullet)][\Theta(\boldsymbol{x}', \bullet)]\right\} \tag{6}$$

For the sake of simplicity, porosity samples are supposed to be independent and identically distributed (*i.i.d.*). Accordingly, for each pair $(\boldsymbol{x}, \boldsymbol{x}')$, fields are assumed to be statistically

independent following a Gaussian probability density function. Therefore, the covariance matrix $\boldsymbol{K}$ is described by a white noise random field proportional to the Dirac-delta function δ

$$\boldsymbol{K}(\boldsymbol{x}, \boldsymbol{x}') \propto \delta(\boldsymbol{x} - \boldsymbol{x}') \tag{7}$$

Overcoming the issue that the white noise variance process is infinite, a grid-based approach is used to approximate the corresponding random field. A concise review on white noise modeling can found in [36].

2.3. Finite element formulation

The mechanical performance of the porous compacts is approximated numerically as an elastic continuum. Therefore, the problem is described by the linear constitutive model presented in Eq. (1). In a deterministic finite element context, the assembled form of the equilibrium equation is expressed as a linear equation system

$$\boldsymbol{K} \cdot \boldsymbol{U} = \boldsymbol{F} \tag{8}$$

where $\boldsymbol{K}$ is the assembled stiffness matrix, $\boldsymbol{U}$ is the nodal displacement vector, and $\boldsymbol{F}$ is the nodal force vector. Nevertheless, since heterogeneity gives rise to response fluctuations, the stiffness matrix can be formulated in terms of the uncertain parameter $\Theta(\boldsymbol{x}, \bullet)$ and the stochastic form of Eq. (8) rewritten as

$$\boldsymbol{U}(\boldsymbol{x}, \Theta) = \boldsymbol{K}^{-1}(\boldsymbol{x}, \Theta) \cdot \boldsymbol{F} \tag{9}$$

where $\boldsymbol{K}^{-1}(\boldsymbol{x}, \Theta)$ is the inverse of the stochastic stiffness matrix. For the sake of simplicity, the force vector $\boldsymbol{F}$ is supposed to be deterministic. From Eq. (9), it seems that uncertainty propagates through the response variability of the system $\boldsymbol{U}(\boldsymbol{x}, \Theta)$ [37, 38].

A Monte Carlo approach uses a sampling method to generate a set of conditional realizations of the field Θ over the probability space. Next, realizations are used as the inputs of the finite element analyses to estimate nodal displacement's variability, *i.e.*, $\boldsymbol{U}(\boldsymbol{x}, \omega)$.

Finally, the stochastic response defines both the strain and stress fields through the kinematic and constitutive equations, respectively.

2.4. Random field discretization

Within the stochastic finite element framework, it requires converting porosity into a discrete spatial distribution. Consequently, the random field $\Theta(\boldsymbol{x}, \bullet)$ characterizes porosity values at discrete points $\boldsymbol{x}$ on D. A discretization scheme uses an unstructured finite element mesh and a structured grid, as schematized in Fig. 4. The unstructured mesh consists of triangular elements and discretizes the specimen and jaws displacement fields. The structured grid comprises quadrilateral elements and discretizes specimen porosity. Thus, porosity is evaluated at each discrete point, assuming its spatial variability as a white noise field defined by a given probability distribution. Porosity at discrete points is chosen independently from values sampled at other points; thus, for an *n*-point mesh, there must be *n* uncorrelated observations. A bilinear interpolation estimates values at unsampled points and ensures that values change continuously within the two-dimensional space. However, gradients change discontinuously at the boundaries of each grid square and the interpolated function is much smoother than the field it approximates. Neither the number nor location of the random field points coincides with their counterpart in the finite element mesh, as shown in Fig. 4. Thus, it is required to map porosity values to each Gaussian-point through the bilinear interpolation scheme when integrating local stiffness matrices. Figure 4b shows an overlaying square grid where closed and open circles represent grid points falling inside and outside the disc's boundary, respectively. Open circles are dummy valued points added to the grid to use the same interpolation scheme for both the interior and the boundary points.

Therefore, given the interpolants f's at surrounding points (x_i, y_j), (x_{i+1}, y_j), (x_i, y_{j+1}), and (x_{i+1}, y_{j+1}) depicted in Fig. 5, the simplest surface between the four vertices is given as

$$f(c_1, c_2) = (1-c_1)(1-c_2) f_{i,j} + c_1(1-c_2) f_{i+1,j} + (1-c_1)c_2 f_{i,j+1} + c_1 c_2 f_{i+1,j+1} \tag{10}$$

where c_1 and c_2 represent bilinear weights, given as

$$c_1 = \frac{x - x_i}{x_{i+1} - x_i} \quad \text{and} \quad c_2 = \frac{y - y_j}{y_{j+1} - y_j} \tag{11}$$

with x and y as the interpolated point coordinates. Thus, any interpolated porosity value is calculated using the interpolants $f_{i,j}$, $f_{i+1,j}$, $f_{i,j+1}$, and $f_{i+1,j+1}$ weighted by c_1 and c_2 [39].

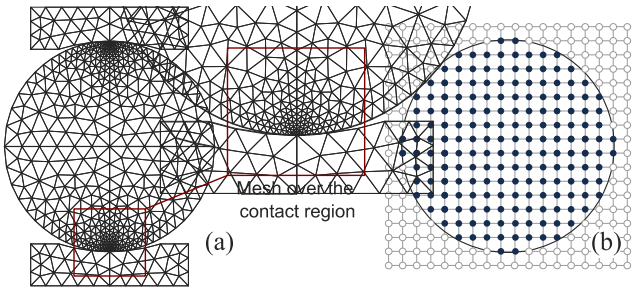

Fig. 4 Two spatial discretization schemes; (a) unstructured finite element mesh with meshing detail over the contact region and (b) structured random field grid

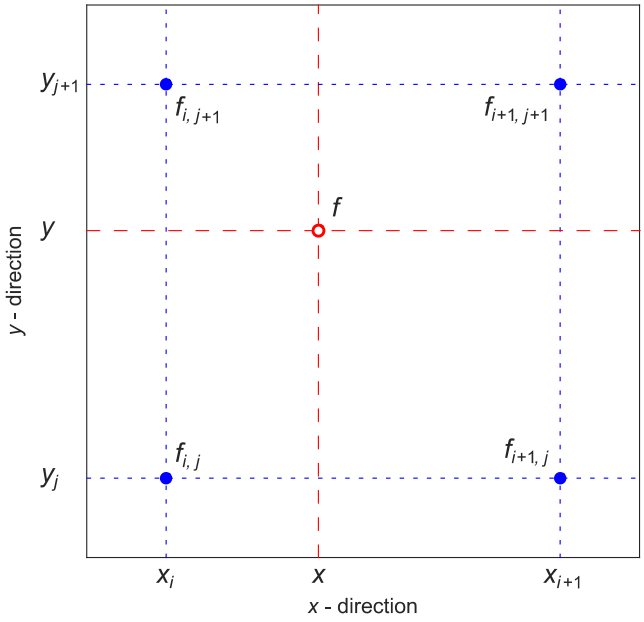

Fig.5 Bilinear interpolation scheme. Blue closed dots correspond to interpolant points and the red open dot represents an interpolated point

3. NUMERICAL EXAMPLES AND DISCUSSION

This section describes the numerical simulations on the behavior of powder materials compacted into macroscopically dense disc-shaped specimens. The diameter and thickness of the discs are 20.0 and 4.0 mm, respectively. The steel loading jaws have radii of curvature of 16.0 mm. The above conditions ensure that reaction loads between the specimen and jaws distribute over small arcs, avoiding unrealistic stress concentrations. Contact is frictionless, and identical boundary and loading conditions apply to all simulations. Thus, horizontal and vertical displacements are completely restrained for the bottom jaw. Similarly, horizontal displacement is restrained at the top jaw while a total vertical displacement of 0.1 mm replicates a monotonic compressive load.

It is assumed that the material exhibits a quasi-brittle linear elastic behavior with porosity as a manufacturing variable. Consequently, neither pore collapse nor flattening at loading points takes place. Likewise, it is expected that the manufacturing process left the material with a non-homogeneous porosity distribution exhibiting a mean value of 0.20. No other defects or residual stresses are considered for the simulations. The mean elastic properties of the fully dense material are elastic modulus of 28.0 MPa and Poisson's ratio of 0.3. The jaws material is steel with an elastic modulus of 210.0 GPa and Poisson's ratio of 0.33.

3.1. Analytical model

The indirect tensile test of homogeneous and isotropic elastic materials has been analytically treated for some authors. Frocht [40] and Timoshenko and Goodier [41] proposed a solution for the stress distributions in discs subjected to a pair of concentrated compressive loads applied across the diameter. According to their model, the $x-$, $y-$, and $xy-$stress components at any point within the discs are described by the following equations

$$\sigma_x = \frac{2P}{\pi Rt}\left\{\frac{1}{2} - \frac{x^2 R(R-y)}{[x^2+(R-y)^2]^2} - \frac{x^2 R(R+y)}{[x^2+(R+y)^2]^2}\right\}$$
$$\sigma_y = \frac{2P}{\pi Rt}\left\{\frac{1}{2} - \frac{R(R-y)^3}{[x^2+(R-y)^2]^2} - \frac{R(R+y)^3}{[x^2+(R+y)^2]^2}\right\}$$
$$\sigma_{xy} = \frac{2P}{\pi Rt}\left\{\frac{xR(R-y)^2}{[x^2+(R-y)^2]^2} + \frac{xR(R+y)^2}{[x^2+(R+y)^2]^2}\right\} \tag{12}$$

where P is the concentrated load, R and t are the radius and thickness, and x and y are the coordinates of the point of interest. Some other closed-form solutions have been proposed in the literature under different boundary conditions [42–44]. It is seen from Eq. (12) that the analytical solution is independent of the elastic properties of the material and is exclusively a function of the force magnitude and disc's dimensions. Likewise, it is obvious from Eq. (12) that the maximum tensile stress takes place at the center of the disc, where the stress state is given as

$$\sigma_x = \sigma_{max} = \frac{P}{\pi Rt}$$
$$\sigma_y = -3\sigma_x = -\frac{3P}{\pi Rt} \tag{13}$$

The compression test concerns itself with the maximum tensile stress reaching a critical value known as indirect tensile strength. It is upon the assumption that the initial crack appears roughly near the center of the disc and propagates along the loading direction. From Eq. (13), the stress state at the center point corresponds to a biaxial one where the compressive component is three times larger than the tensile one and where the shear stress vanishes. Therefore, it is expected that due to opposite sign stresses, indirect tensile strengths determined from the Brazilian test could be slightly higher than the ones obtained from direct tensile tests [45, 46].

Figure 6 shows qualitative contour plots of the x–, y–, and xy – stress components according to the analytical solution for the homogenous case given in Eq. (12) and normalized by the maximum tensile stress σ_{max}, according to Eq. (13).

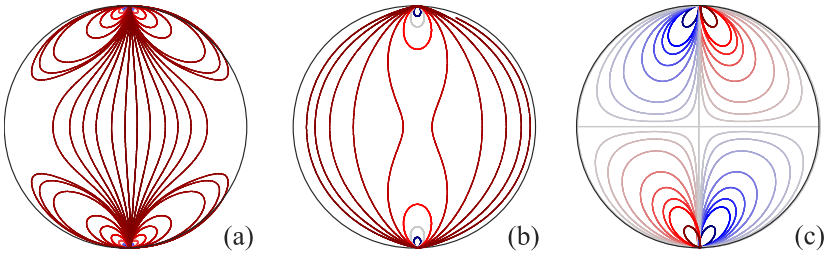

Fig. 6 Qualitative contour plots of the (a) $x-$, (b) $y-$, and (c) $xy-$stress components for the theoretical homogeneous case

3.2. Deterministic numerical analysis

The numerical setup validity is first assessed through the predicted stress distributions and maximum stress values, neglecting uncertainties. Thus, let us analyze the test under the assumption that porous material properties correspond to a case restricted to average values and that boundary conditions match the test operating conditions. This deterministic case qualitatively compares the numerical stress distributions with the analytical ones proposed by Frocht [40] and normalizes the results obtained in the stochastic analysis described in the last part of this section. An unstructured mesh with Lagrange triangular elements discretizes the problem domain, as shown in Fig. 4a. Respectively, a total of 1016 and 140 elements are used for the specimen and jaw meshes. Figure 7 display the predicted $x-$, $y-$, and $xy-$stress distributions within the disc specimen. Comparing the analytical and numerical distributions of Figs. 6 and 7, these seem to be consistent for the three stress components. Distribution discrepancies are unsurprisingly larger in the loading zone vicinity, where prescribed conditions are different between the cases. The largest theoretical to numerical $x-$, $y-$, and $xy-$stress ratios were respectively 68.7, 14.6, and 780.6. Correspondingly, the stress ratios at the center of the disc equal 1.0 for all three components with maximum tensile and compressive stresses of 13.71 and 41.13 MPa, respectively. Both solutions are consistent for points far from the loading zones, proving that boundary conditions do not play a major role in the stress distributions.

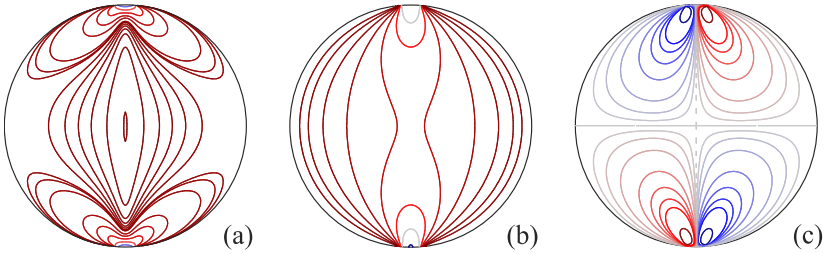

Fig. 7 Qualitative contour plots of the (a) $x-$, (b) $y-$, and (c) $xy-$stress components for the numerical homogeneous case

3.3. Stochastic analysis

Analytical stress distributions do not suit heterogeneous materials. The closed-form solution in the "Analytical model" section is independent of the elastic properties; though, it is expected stress variability to intensify with heterogeneity. Hence, different realizations are generated to study the relations between porosity and behavior at the macroscopic scale. In this section, the formulation introduces porosity according to its spatial fluctuation. The analysis considers two case studies to investigate solution dependency on porosity. Each analysis with 1000 realizations represents correspondingly a somewhat homogeneous material and a more heterogeneous one. Following Wachtman [47] and Ashkin [48], the relationship between porosity and the elastic modulus is treated as linear and quantitatively deterministic; therefore,

$$E = E_0(1.0 - 1.9\theta) \tag{14}$$

where E_0 is the elastic modulus of the fully dense material and θ is the local porosity. Other empirical relationships can be found in [49–52].

The numerical simulations use the two-dimensional fields described in the "Description of the random porosity field" section. The mean μ_θ and coefficient of variation δ_θ of each realization specify the inherent porosity variability. A stream of porosity values

ω is randomly chosen from the standard Gaussian probability function for each sample point. Then, $\boldsymbol{\theta}(\boldsymbol{x},\omega)$ is a vector of uncorrelated random porosity values such as [53]

$$\boldsymbol{\theta}(\boldsymbol{x},\omega) = \mu_\theta[1+\delta_\theta \boldsymbol{\varsigma}(\boldsymbol{x},\omega)] \tag{15}$$

where $\boldsymbol{\varsigma}(\boldsymbol{x},\omega)$ is a zero-mean vector of uncorrelated Gaussian random variables; thus, $\delta_\theta \boldsymbol{\varsigma}(\boldsymbol{x},\omega)$ represents porosity fluctuation about the mean value μ_θ. Figure 8 presents a random field realization in an 18-by-18-point grid with a mean porosity of 0.20 and a coefficient of variation of 10%. Specifically, results in Fig. 8a show interpolant points within the sampling space where the different colors approximate discrete porosity values. Figure 8b displays the corresponding interpolated random field.

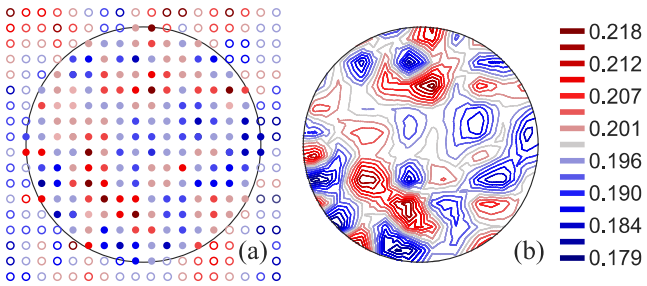

Fig. 8 Porosity field realization. (a) Discrete interpolant points and (b) interpolated random field

Figures 9a and 9b show in light gray the probability distribution streams for both case studies. These distributions were generated from observations at 961 integration points via the specified porosity-elastic modulus relationship given in Eq. (14). The population means are shown in dark red in Figs 9a and 9b, where each one has an estimated mean modulus of 20.0 GPa and coefficients of variation of 10% for the first case study and 20% for the second one.

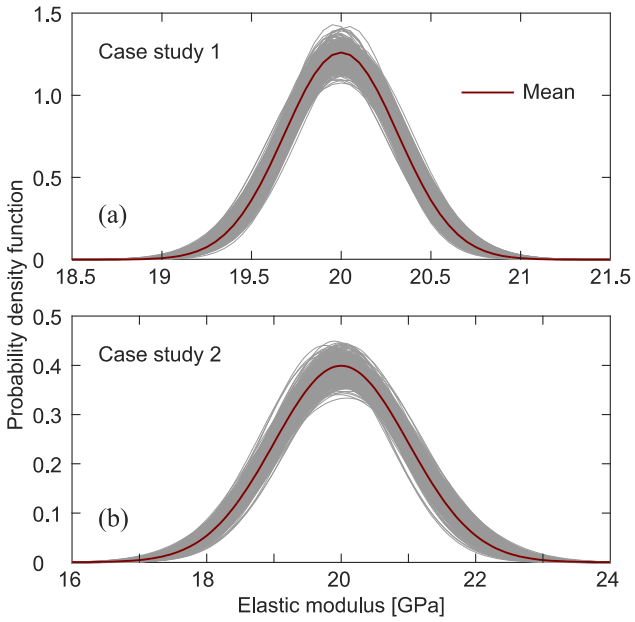

Fig. 9 Predicted probability density functions for the elastic modulus for (a) case study 1 and (b) case study 2

As pointed out above, experimental test success is achieved when the first signs of damage appear someplace near the specimen's center. Bearing that in mind, the first goal is to analyze the predicted tensile stresses. Thus, numerical outcomes are evaluated considering a stochastic approach, prior knowledge of porosity variance. First, comparing a selection of numerical samples, Figs. 10 and 11 illustrate two porosity field realizations of case studies 1 and 2 and the corresponding qualitative $x-$, $y-$, and $xy-$ stress distributions. Porosity fields shown in Fig. 10a and 11a correspond to the ones used to estimate the corresponding stress distributions when the mean coefficients of variation are 10% and 20%, respectively. For the first case, porosity ranges from 0.192 to 0.208; for the second one, it varies over a wider range from 0.174 to 0.229. Different to distributions in Figs. 6 and 7, distributions from Figs. 10 and 11 are asymmetrical along the loading plane and exhibit sudden changes. Likewise, comparing Figs. 10 and 11, field distortions are greater along the loading plane when porosity variance increases, reflecting the influence of more heterogeneous material. Then, Figs. 10b and 11b show the location where the crack could initiate and develop. The maximum values do not appear at the center of the disc for any of the distributions. For the first case, the

highest tensile stress is equal to 13.9 MPa, and its location is on the loading plane; even so, it deviates from the horizontal diameter. For the second case, the maximum tensile stress is equal to 14.7 MPa, and its location departs from the loading plane and more significantly from the horizontal diameter.

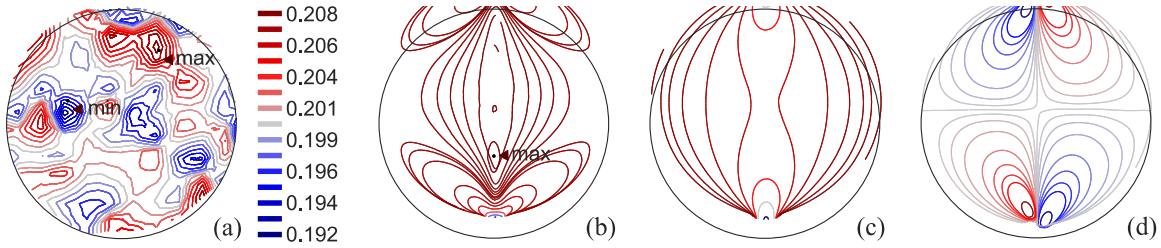

Fig. 10 (a) Porosity field realization of a heterogeneous material from case study 1 and the corresponding qualitative stress fields of the (b) $x-$, (c) $y-$, and (d) $xy-$components

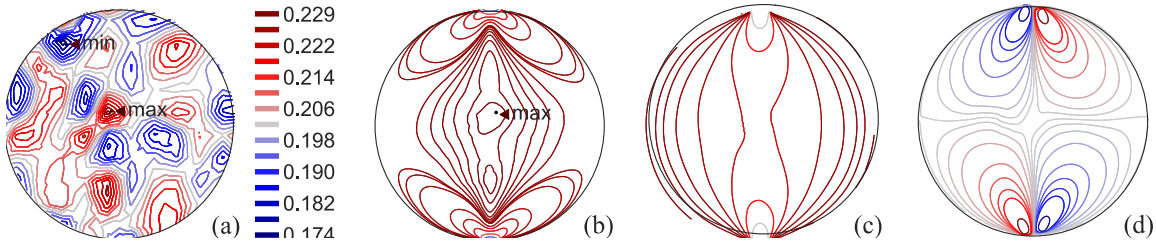

Fig. 11 (a) Porosity field realization of a heterogeneous material from case study 2 and the corresponding qualitative stress fields of the (b) $x-$, (c) $y-$, and (d) $xy-$components

Scatter plots in Fig. 12 summarize 1000 realizations of the predicted maximum tensile stress normalized to the corresponding theoretical value of 13.71 MPa. From Fig. 12, most realizations show maximum values above the theoretical one. For the first case study in Fig. 12a, 977 out of 1000 realizations exceed the stress ratio of 1.0, where the largest stress ratio equals 1.04. On the other hand, the number of realizations beyond the threshold rises to 993, and the largest stress ratio equals 1.16 for the second case.

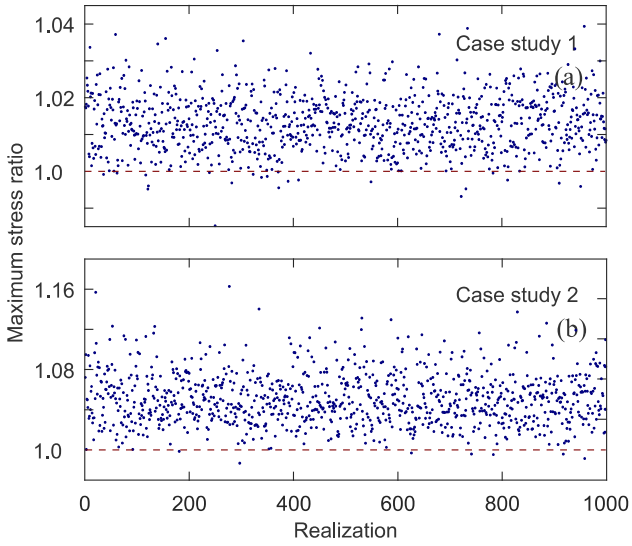

Fig. 12 Scatter plot of the maximum tensile stress ratios for case studies (a) 1 and (b) 2

Likewise, Fig. 13 presents the convergence analysis of the numerical outcomes. The plots depict the stress ratio mean and coefficient of variation versus the number of simulation runs for both case studies. From the results, it is seen convergence after 600 realizations. For the total realization number, the means and coefficients of variation are respectively 1.013 and 1.01% for the first case study and are 1.051 and 2.47% for the second one. For both cases, mean ratios are fairly close to 1.0; however, both means and variations increase as porosity heterogeneity evolves.

Figure 14 depicts the empirical cumulative density functions for the predicted stress ratios. These density functions correspond to the upper and lower bounds resulting from the propagation of porosity uncertainties. Likewise, Fig. 14 overlays as dashed lines the theoretical normal cumulative functions based on the outcome means of [1.013, 1.051] and coefficients of variation of [1.01, 2.47] %. As expected, empirical and theoretical functions overlay quite close. From the cumulative function, the drawn maximum tensile stress ratios on the 5%, 50% and 95% quantile are [1.0015, 1.0137], [1.0128, 1.0479], and [1.0261, 1.0970], respectively.

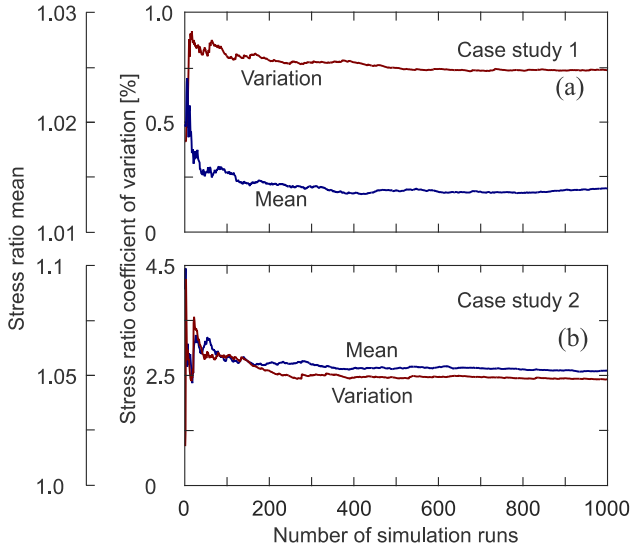

Fig. 13 Convergence test for the stress ratio mean and coefficient of variation for case studies (a) 1 and (b) 2

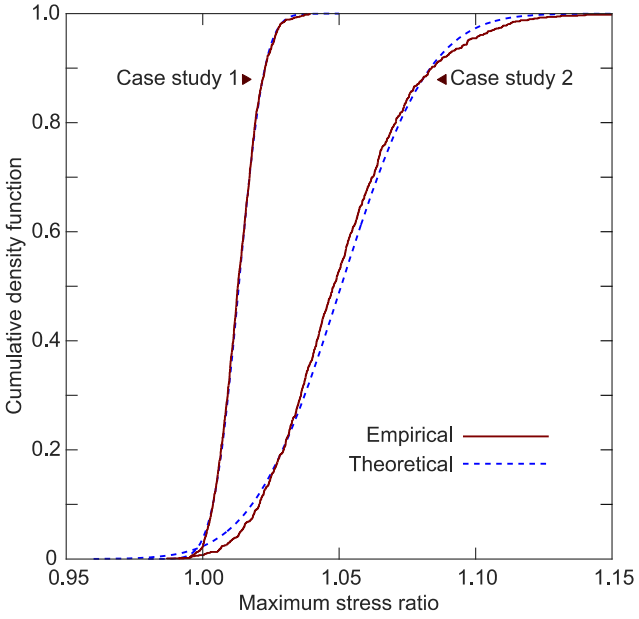

Fig. 14 Cumulative density function of the maximum tensile stress ratio for case studies 1 and 2

Statistical distributions for the location of the predicted maximum tensile stresses are also presented. Figure 15 graphically compares the location departure from the specimen's center for the two case studies and shows the corresponding theoretical probability distributions for the normalized diameters. Probability distributions are plotted against a normal distribution, where for the vertical case, distributions are truncated to the specified diameter limits. The distributions reveal a significant porosity heterogeneity influence on the maximum tensile stress location during the test. The most noteworthy feature is the deviation of the horizontal location from the loading plane as porosity variance increases. However, it is apparent from the distributions and the point patterns that location variances are larger for the vertical direction when compare to the horizontal one.

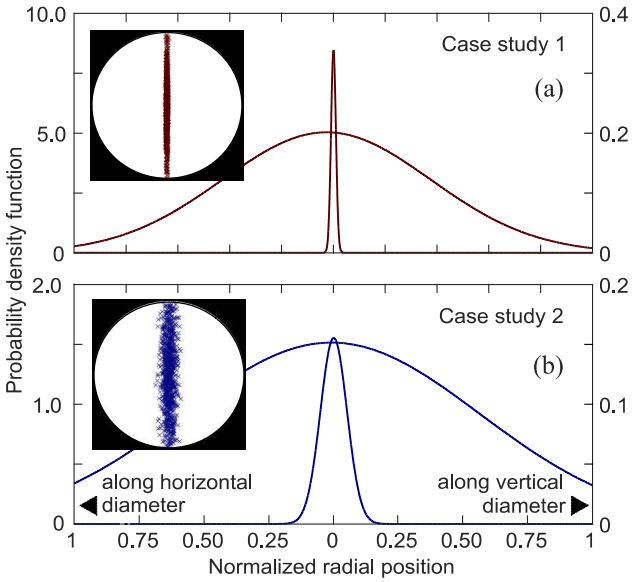

Fig. 15 Statistical distributions for the location of the predicted maximum tensile stresses for case studies (a) 1 and (b) 2

CONCLUSIONS

This work presented a stochastic assessment of the impact of material heterogeneity on the mechanical performance of the diametral compression test of powder compacts and porous materials. In the proposed stochastic formulation, a random spatial field described porosity

variability, and a finite element solved the constitutive model. Two numerical case studies captured the influence of porosity uncertainties on the magnitude and location of the maximum tensile stress within disc-shaped specimens. Comparisons with analytical and deterministic models for homogeneous samples were presented. Simulation outcomes indicate that for heterogeneous powder compacts, the maximum tensile stress exhibits random fluctuations both in magnitude and location, which affect test accuracy as porosity spatial variability increases. From the findings, it is seen that the proposed model can be used to gain insight into the validity of the diametral compression test as an indirect technique to estimate the tensile strengths of quasi-brittle material exhibiting porosity heterogeneity.

ACKNOWLEDGEMENTS

The authors acknowledge the University of the Andes for a sabbatical leave granted to JA Alvarado-Contreras.

DECLARATIONS

Funding

No funding was received for conducting this study.

Conflicts of Interest/Competing Interests

To the knowledge of the authors, there are no conflicts of interest or competing interests for this paper.

Availability of data and material

Data and material written in this study is available upon request to the corresponding author.

Code Availability

Code written in this study is available upon request to the corresponding author.

Authors' contributions

All authors contributed to the study's conception and design. Material preparation, data collection, and analysis were performed by J.A. Alvarado-Contreras and A.A. López-Inojosa. The first draft of the manuscript was written by J.A. Alvarado-Contreras and all authors commented on previous versions of the manuscript. All authors read and approved the final manuscript.

Ethics approval

Not applicable.

Consent to participate

Not applicable.

Consent for publication

Not applicable.

Financial interests

The authors have no relevant financial interests to disclose.

REFERENCES

[1] Gunathilake TMSU, Ching YC, Ching KY, Chuah CH, Abdullah LC (2017) Biomedical and microbiological applications of bio-based porous materials: A review. Polymers. https://doi.org/10.3390/polym9050160

[2] George N, Nair AB (2018) Porous tantalum: A new biomaterial in orthopedic surgery. In: Preetha B, Sreekala MS, Sabu T (eds) Fundamental Biomaterials: Metals. Woodhead Publishing, Cambrigde, pp 243–268. https://doi.org/10.1016/B978-0-08-102205-4.00011-8

[3] Lascano S, Arévalo C, Montealegre-Melendez I, Muñoz S, Rodriguez-Ortiz JA, Trueba P, Torres Y (2019) Porous titanium for biomedical applications: Evaluation of the conventional powder metallurgy frontier and space-holder technique. Appl Sci. https://doi.org/10.3390/app9050982

[4] Kakar S, Einhorn TA (2004) Tissue engineering of bone. In: Hollinger JO, Einhorn TA, Doll BA, Sfeir C (eds) Bone Tissue Engineering. CRC Press, Boca Raton, pp 277–302.

[5] Hudecki A, Kiryczyński G, Łos MJ (2019) Biomaterials, definition, overview, In: Łos MJ, Hudecki A, Wiecheć E (eds) Stem Cells and Biomaterials for Regenerative Medicine. Academic Press, London, pp 85–98. https://doi.org/10.1016/B978-0-12-812258-7.00007-1

[6] Ralls A, Kumar P, Misra M, Menezes PL (2020) Material design and surface engineering for bio-implants. JOM-J Min Met Mat S. https://doi.org/10.1007/s11837-019-03687-2

[7] Rubow KL (2009) Porous metals for aerospace. Adv Mater Process 167:26–28

[8] Ishizaki K, Komarneni S, Nanko M (1998) Powder compacts and green bodies for porous materials, In: Ford RG (ed) Porous Materials. Materials Technology Series. Springer, Boston, pp 12–37. https://doi.org/10.1007/978-1-4615-5811-8_2

[9] Bolat Ç, Akgün İC, Göksenli, A (2020) On the way to real applications: Aluminum matrix syntactic foams. EMS. https://doi.org/10.26701/ems.703619

[10] Yuan H, Zhang L, Ma S (2019) Damage evolution and characterization for sintered powder metals with the varying porosity. Eng Fract Mech. https://doi.org/10.1016/j.engfracmech.2018.12.014

[11] Skorokhod VV, Olevskii EA, Shtern MB (1993) Continuum theory of sintering. III. Effect of inhomogeneous distribution of properties in compacts and of pressing conditions on the kinetics of sintering. Powder Metall Met Ceram. https://doi.org/10.1007/BF00559750

[12] Wang C, Chen SH (2012) The influence of agglomerates on the densification and microstructural evolution in sintering of a multi-particle system. Sci China-Phys Mech Astron. https://doi.org/10.1007/s11433-012-4743-4

[13] Magdeski JS (2010) The property dependence of mechanical properties of sintered alumina. J Univ Chem Technol Metallurgy 45, 143-148

[14] Carneiro FLLB (1943) A new method to determine the tensile strength of concrete. In: Proceedings of the 5th Meeting of the Brazilian Association for Technical Rules. Associação Brasileira de Normas Técnicas, Rio de Janeiro, pp 126–129

[15] Franklin JA (1985) Suggested method for determining point load strength. Int J Rock Mech Min Sci. https://doi.org/10.1016/0148-9062(85)92327-7

[16] Li D, Wong LNY (2013) The Brazilian disc test for rock mechanics applications: Review and new insights. Rock Mech Rock Eng. https://doi.org/10.1007/s00603-012-0257-7

[17] Hangl M, Börger A, Danzer R, Luxner HM (2002) Application of the Brazilian disc test for strength measurements on ceramic green bodies. In: Bradt RC, Munz D, Sakai M, Shevchenko VY, White K (eds) Fracture Mechanics of Ceramics. Springer, Boston, pp 159-167. https://doi.org/10.1007/978-1-4757-4019-6_12

[18] Huang SH, Lin LS, Rudney J, Jones R, Aparicio C, Lin CP, Fok A (2012) A novel dentin bond strength measurement technique using a composite disk in diametral compression. Acta Biomater. https://doi.org/10.1016/j.actbio.2011.12.036

[19] Yohannes B, Gonzalez M, Abebe A, Sprockel O, Nikfar F, Kang S, Cuitino AM (2015) The role of fine particles on compaction and tensile strength of pharmaceutical powders. Powder Technol. https://doi.org/10.1016/j.powtec.2015.01.035

[20] Scapin M, Peroni L, Avalle M (2017) Dynamic Brazilian test for mechanical characterization of ceramic ballistic protection. Shock Vib. https://doi.org/10.1155/2017/7485856

[21] Zhang Q, Zhang XP, Ji PQ (2018) Reducing the anisotropy of a Brazilian disc generated in a bonded-particle model. Acta Mech Sin. https://doi.org/10.1007/s10409-018-0754-3

[22] Mehrabian A, Abousleiman YN (2020) Poroelastic solution to the Brazilian test. Int J Rock Mech Min Sci. https://doi.org/10.1016/j.ijrmms.2019.104201

[23] Yue ZQ, Chen S, Tham LG (2003) Finite element modeling of geomaterials using digital image processing. Comput Geotech. https://doi.org/10.1016/S0266-352X(03)00015-6

[24] Jonsén P, Häggblad HÅ, Sommer K (2007) Tensile strength and fracture energy of pressed metal powder by diametral compression test. Powder Technol. https://doi.org/10.1016/j.powtec.2007.02.030

[25] Jonsén P, Häggblad HÅ (2007) Fracture energy based constitutive models for tensile fracture of metal powders. Int J Solids Struct. https://doi.org/10.1016/j.ijsolstr.2007.02.030

[26] Korachkin D, Gethin DT, Lewis RW, Tweed JH, Guyoncourt DMM (2008) Measurement of Young's modulus and tensile failure properties of green powder compacts. Powder Metall. https://doi.org/10.1179/174329008X284994

[27] Seeber B, Gonzenbach U, Gauckler L (2013) Mechanical properties of highly porous alumina foams. J Mater Res. https://doi.org/10.1557/jmr.2013.102

[28] Cui Z, Huang Y, Liu H (2017) Predicting the mechanical properties of brittle porous materials with various porosity and pore sizes. J Mech Behav Biomed Mater. https://doi.org/10.1016/j.jmbbm.2017.02.014

[29] Coble RL, Kingery WD (1956) Effect of porosity on physical properties of sintered alumina. J Am Ceram Soc. https://doi.org/10.1111/j.1151-2916.1956.tb15608.x

[30] MacKenzie JK (1950) The elastic constants of a solid containing spherical holes. Proc Phys Soc B. https://doi.org/10.1088/0370-1301/63/1/302

[31] Sotomayor OE, Tippur HV (2014) Role of regularity and relative density on elasto-plastic compression response of random honeycombs generated using Voronoi diagrams. Int J Solids Struct. https://doi.org/10.1016/j.ijsolstr.2014.07.009

[32] Geers MGD, Yvonnet J (2016) Multiscale modeling of microstructure-property relationship. MRS Bulletin. https://doi.org/10.1557/mrs.2016.165

[33] Zhu W, Blal N, Cunsolo S, Baillis D (2017) Micromechanical modeling of effective elastic properties of open-cell foam. Int J Solids Struct. https://doi.org/10.1016/j.ijsolstr.2017.02.031

[34] Grigoriu M (2012) Stochastic Systems: Uncertainty Quantification and Propagation 1st edn. Springer-Verlag, London

[35] VanMarcke E (1988) Random Fields: Analysis and Synthesis 3rd edn. The MIT Press, Massachusetts

[36] Gunzburger MD, Webster CG, Zhang G (2014) Stochastic finite element methods for partial differential equations with random input data. Acta Numer. https://doi.org/10.1017/S0962492914000075

[37] Eiermann M, Ernst OG, Ullmann E (2007) Computational aspects of the stochastic finite element method. Comput Visual Sci. https://doi.org/10.1007/s00791-006-0047-4

[38] Ghanem RG, Spanos PD (2012) Stochastic Finite Elements: A Spectral Approach. Dover Publications, New York

[39] Press WH, Teukolsky SA, Vetterling WT, Flannery BP (2007) Numerical Recipes: The Art of Scientific Computing 3rd edn. Cambridge University Press, New York

[40] Frocht MM (1969) Isopachic stress patterns, In: Leven MM. (ed) Photoelasticity. The Selected Scientific Papers of MM Frocht. Pergamon Press, Oxford, pp 137–157. https://doi.org/10.1016/B978-0-08-012998-3.50014-8

[41] Timoshenko SP, Goodier JN (1970) Theory of Elasticity 3rd edn. McGraw-Hill, New York

[42] Hondros G (1959) The evaluation of Poisson's ratio and the modulus materials of a low tensile resistance by the Brazilian (indirect tensile) test with particular reference to concrete. Aust J Appl Sci 10:243–268

[43] Ma CC, Hung KM (2008) Exact full-field analysis of strain and displacement for circular disks subjected to partially distributed compressions. Int J Mech Sci. https://doi.org/10.1016/j.ijmecsci.2007.06.005

[44] Gutiérrez-Moizant R, Ramírez-Berasategui M, Santos-Cuadros S, García-Fernández SS (2020) A novel analytical solution for the Brazilian test with loading arcs. Math Probl Eng. https://doi.org/10.1155/2020/2935812

[45] Efimov VP (2009) The rock strength in different tension conditions. J Min Sci. https://doi.org/10.1007/s10913-009-0071-0

[46] Fuenkajorn K, Klanphumeesri S (2011) Laboratory determination of direct tensile strength and deformability of intact rocks. Geotech Test. https://doi.org/10.1520/GTJ103134

[47] Wachtman JB (1963) Elastic deformation of ceramics and other refractory materials, In: Wachtman JB (ed) Mechanical and Thermal Properties of Ceramics. NBS Special Publication 303, Washington, pp 139–168

[48] Ashkin D, Haber RA, Wachtman JB (1990) Elastic properties of porous silica derived from colloidal gels. J Am Ceram Soc. https://doi.org/10.1111/j.1151-2916.1990.tb06464.x

[49] Gibson LJ, Ashby MF (1982) The mechanics of three-dimensional cellular materials. Proc R Soc Lond. https://doi.org/10.1098/rspa.1982.0088

[50] Ramakrishnan N, Arunachalamt VS (1993) Effective elastic moduli of porous ceramic materials. J Am Ceram Soc. https://doi.org/10.1111/j.1151-2916.1993.tb04011.x

[51] Yoshimura HN, Molisani AL, Narita NE, Cesar PF, Goldenstein H (2007) Porosity dependence of elastic constants in aluminum nitride ceramics. Mater Res. https://doi.org/10.1590/S1516-14392007000200006

[52] German RM (2014) Sintering from Empirical Observations to Scientific Principles. Elsevier, Oxford

[53] Haldar A, Mahadevan S (2000) Probability, Reliability, and Statistical Methods in Engineering Design. John Wiley and Sons, New York

Figures

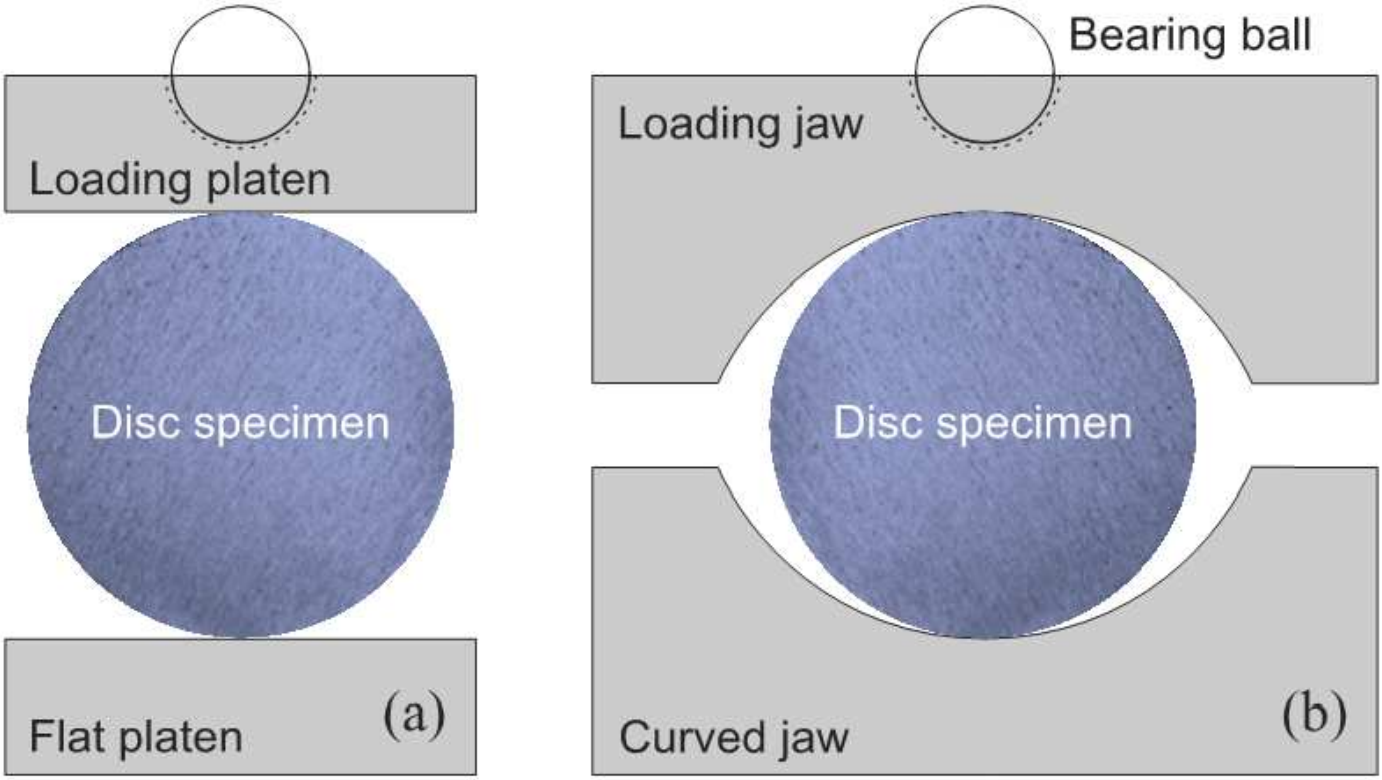

Figure 1

Experimental setups using (a) standard flat loading platens and (b) curved loading jaws

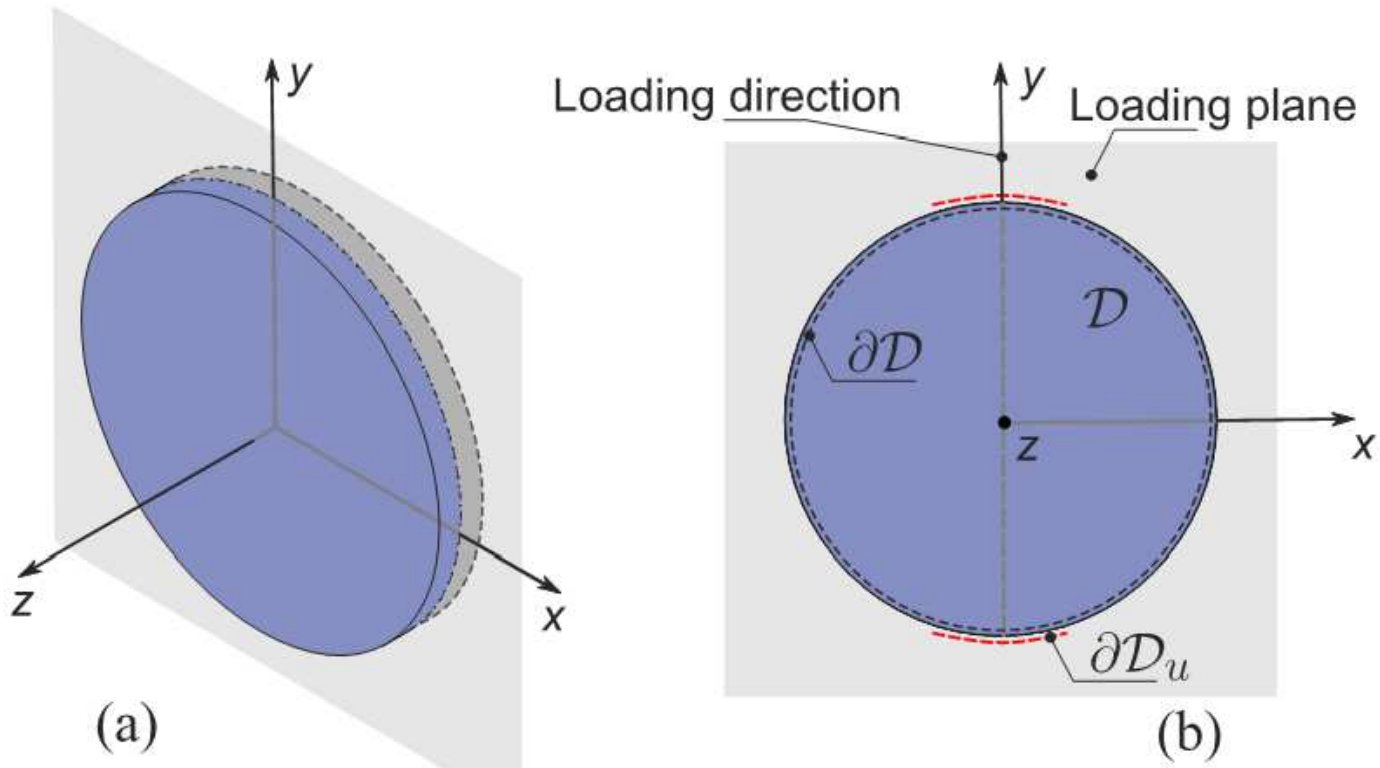

Figure 2

(a) Three-dimensional specimen domain and (b) two-dimensional modeling domain

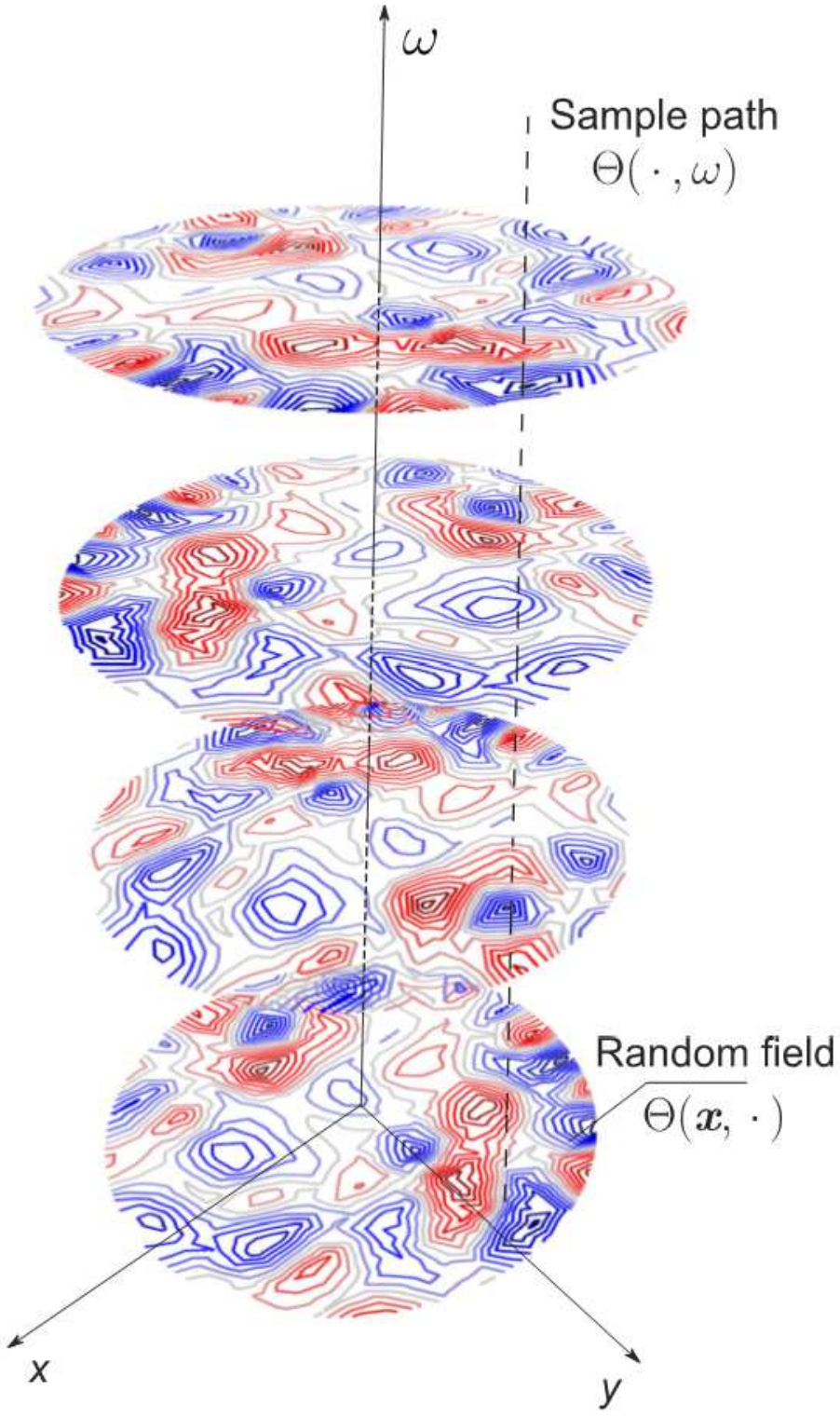

Figure 3

A selection of realizations in the porosity space

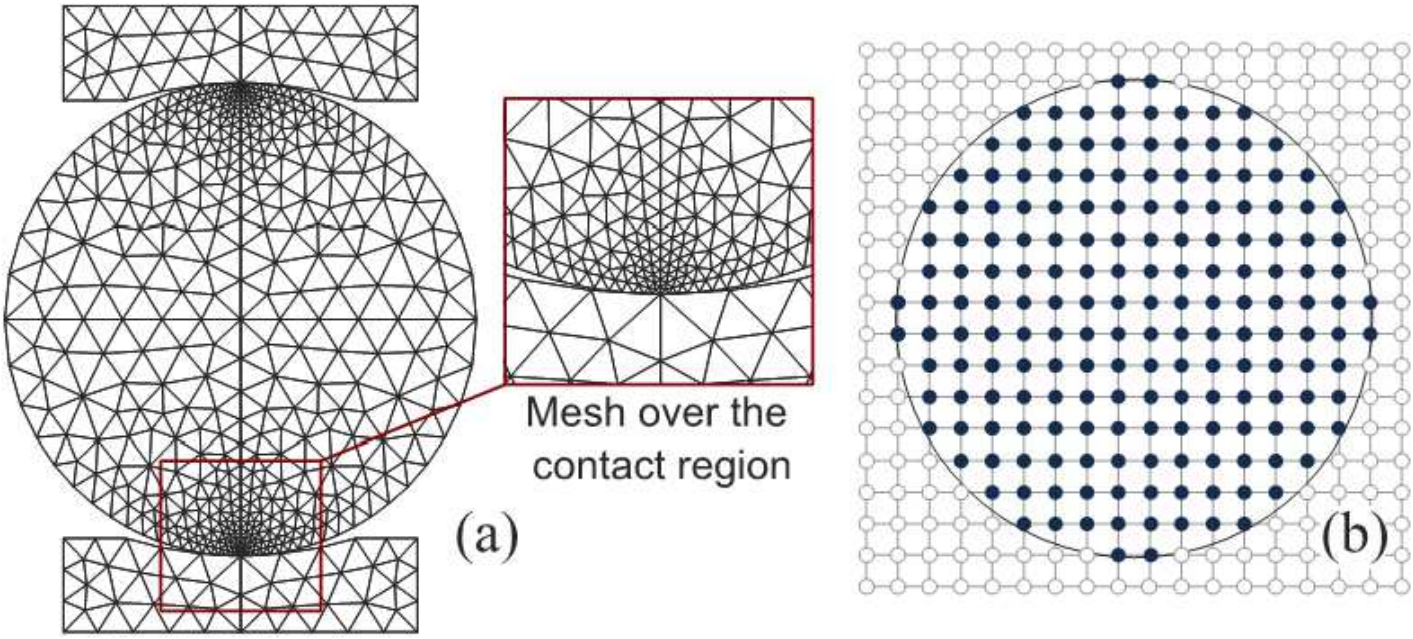

Figure 4

Two spatial discretization schemes; (a) unstructured finite element mesh with meshing detail over the contact region and (b) structured random field grid

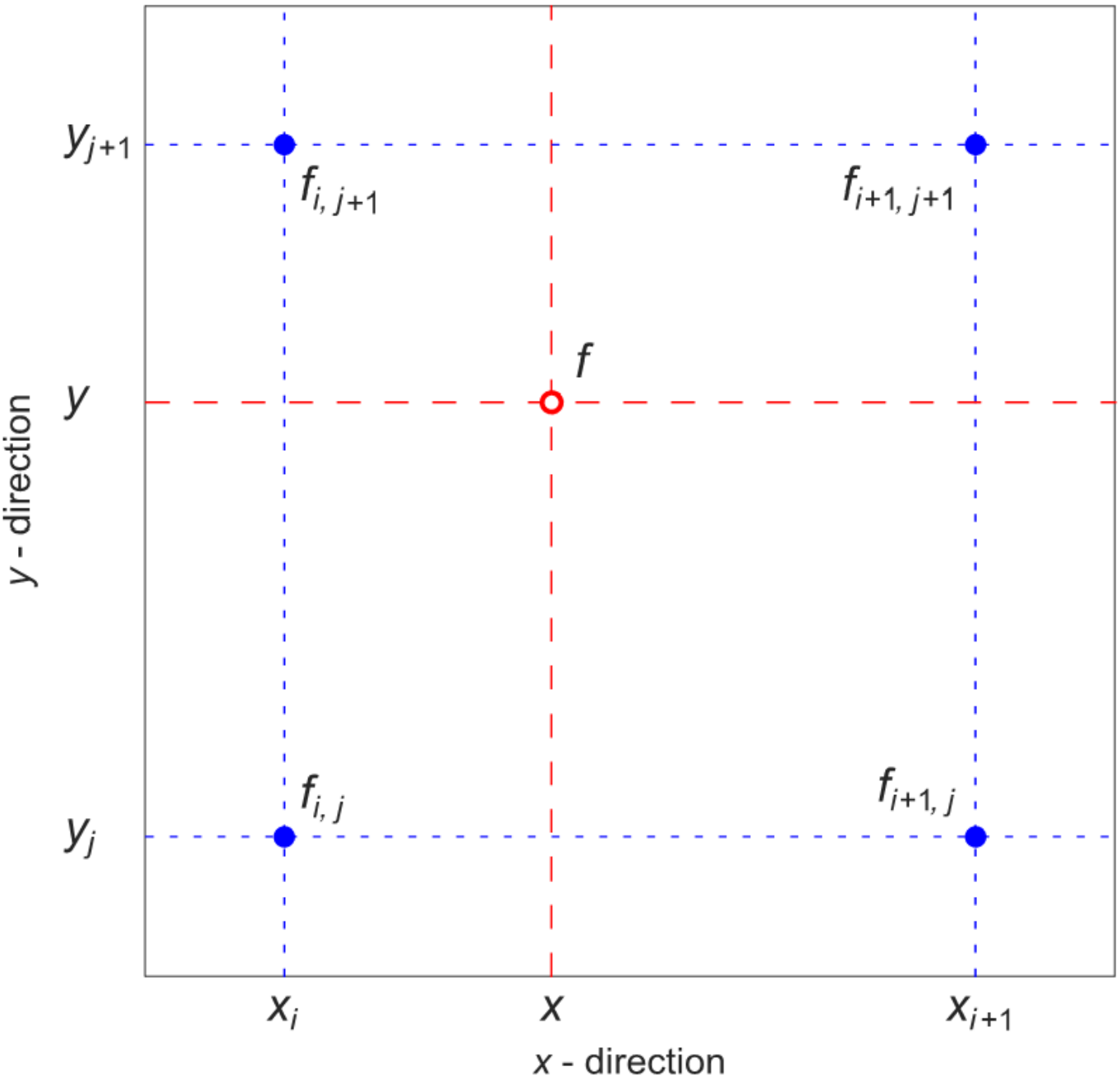

Figure 5

Bilinear interpolation scheme. Blue closed dots correspond to interpolant points and the red open dot represents an interpolated point

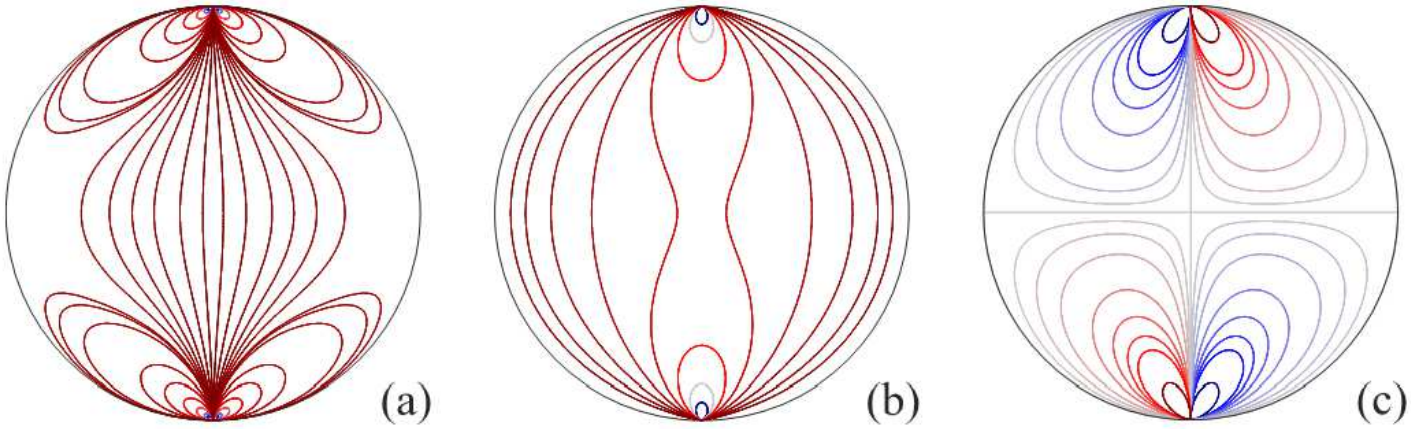

Figure 6

Qualitative contour plots of the (a) x- (b) y- and (c) xy- stress components for the theoretical homogeneous case

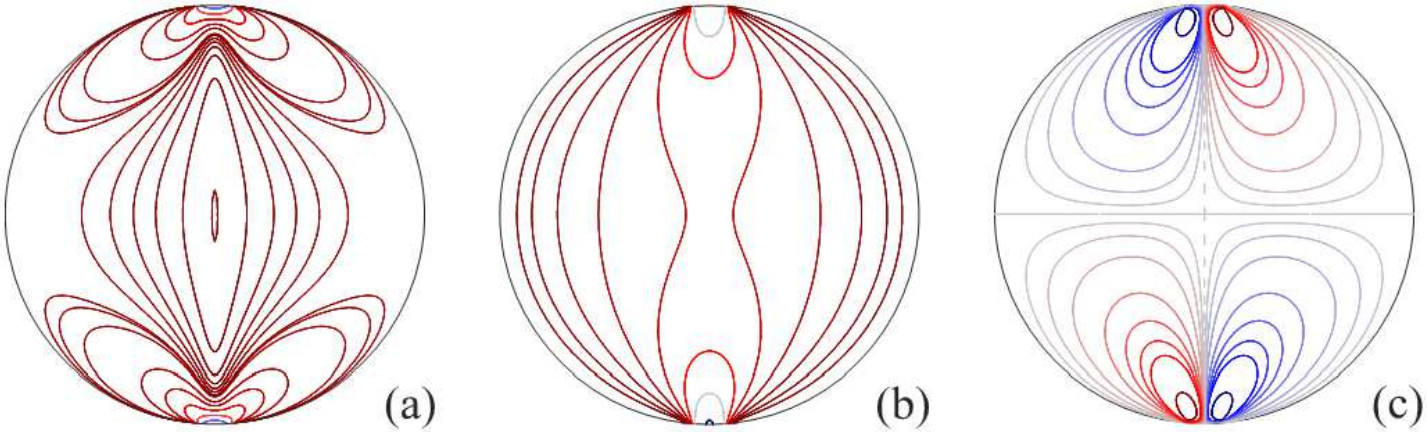

Figure 7

Qualitative contour plots of the (a) x- (b) y- and (c) xy- stress components for the numerical homogeneous case

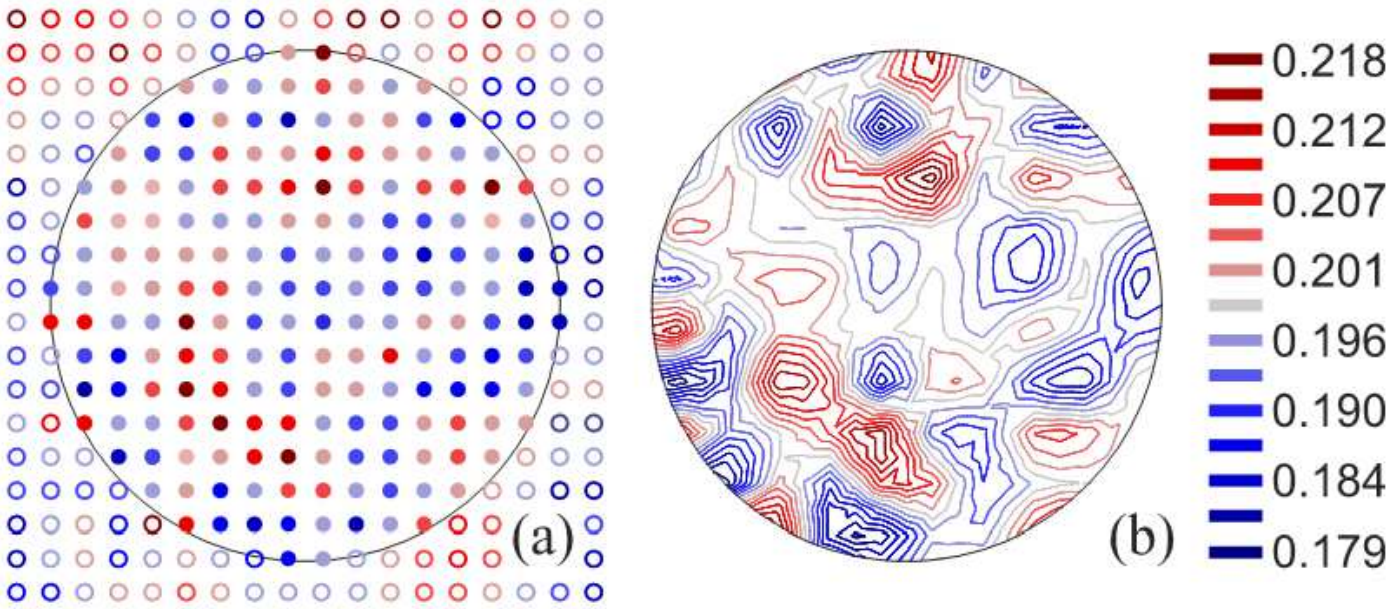

Figure 8

Porosity field realization. (a) Discrete interpolant points and (b) interpolated random field

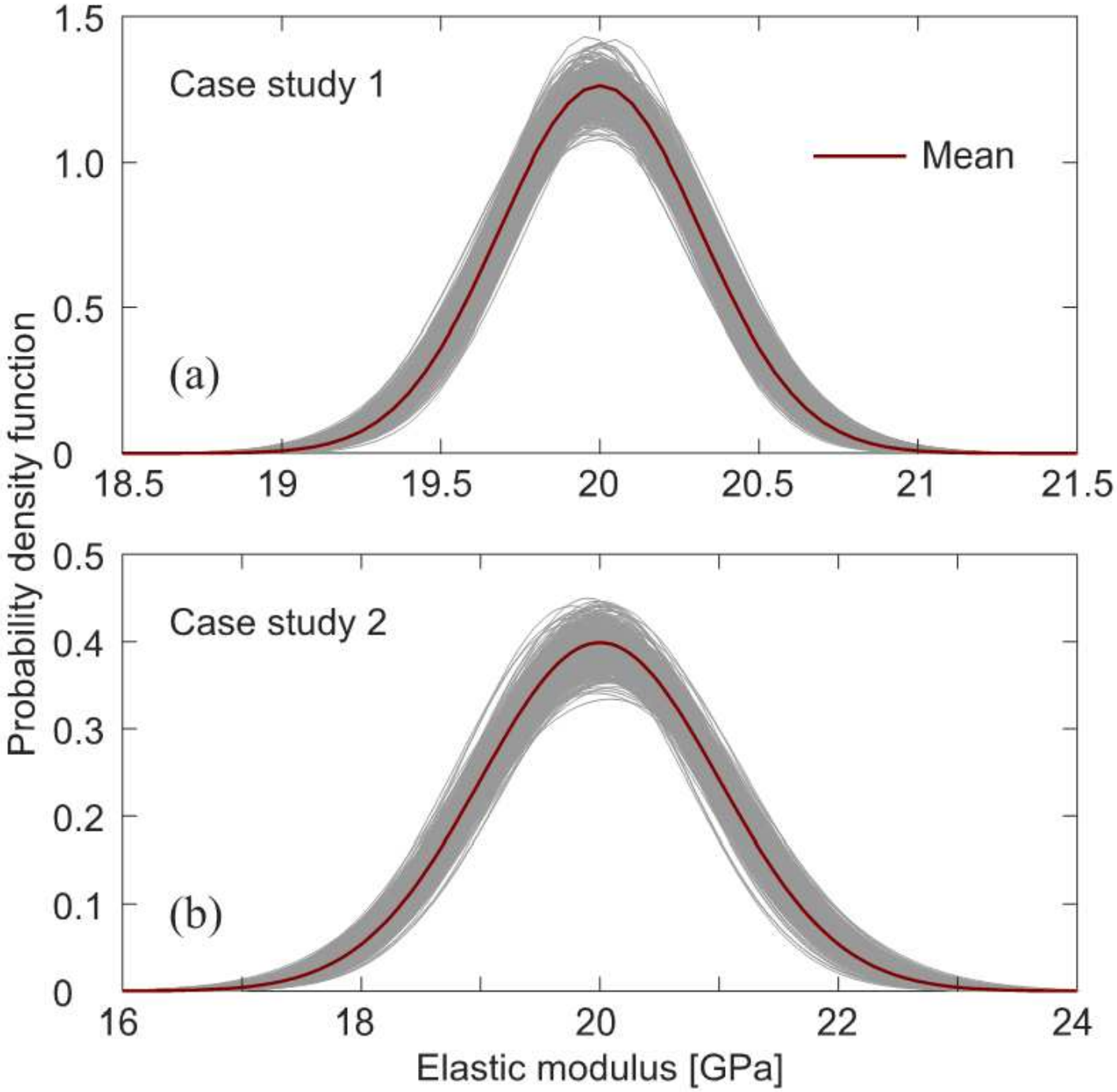

Figure 9

Predicted probability density functions for the elastic modulus for (a) case study 1 and (b) case study 2

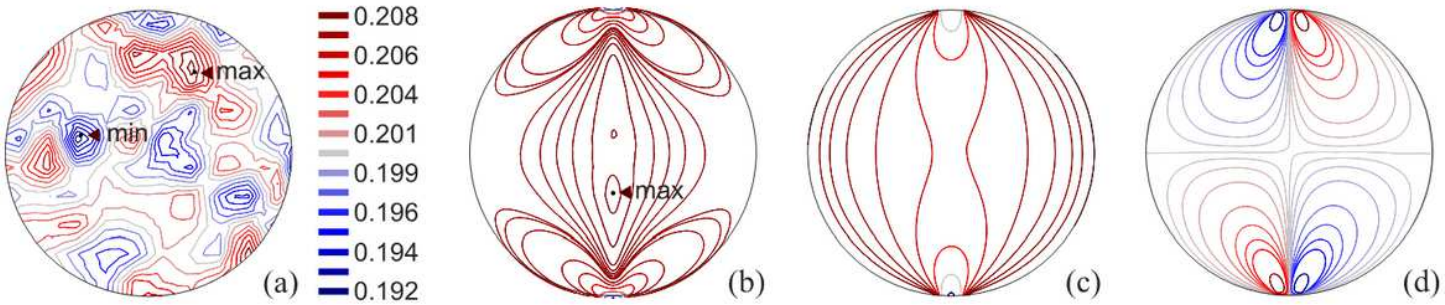

Figure 10

(a) Porosity field realization of a heterogeneous material from case study 1 and the corresponding qualitative stress fields of the (b) x- (c) y- and (d) xy- components

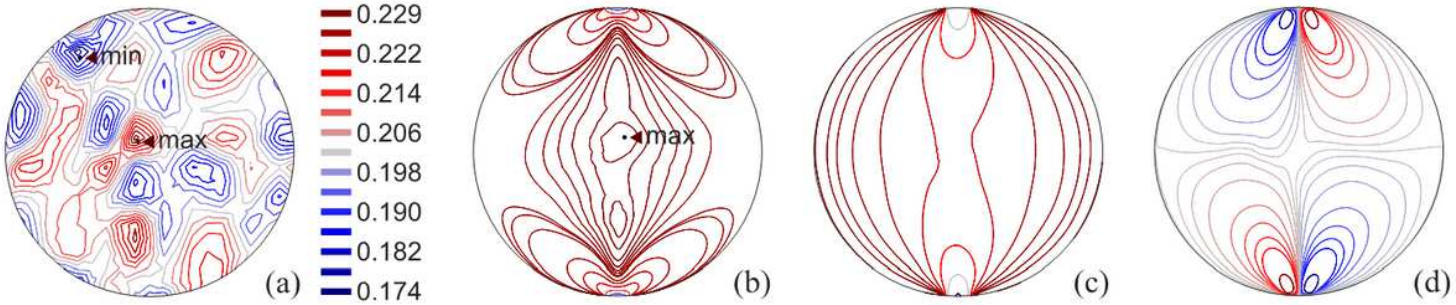

Figure 11

(a) Porosity field realization of a heterogeneous material from case study 2 and the corresponding qualitative stress fields of the (b) x- (c) y- and (d) xy- components

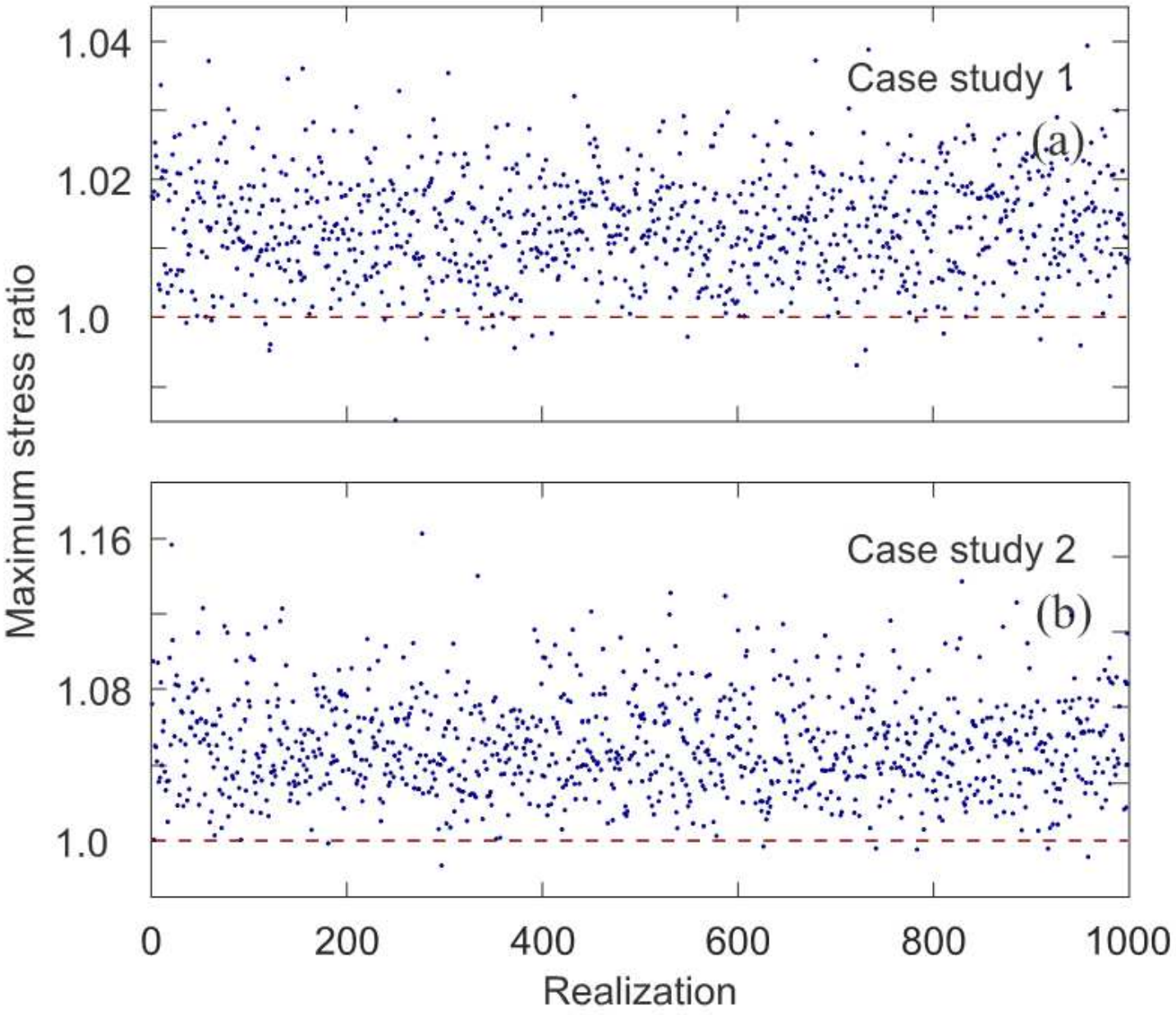

Figure 12

Scatter plot of the maximum tensile stress ratios for case studies (a) 1 and (b) 2

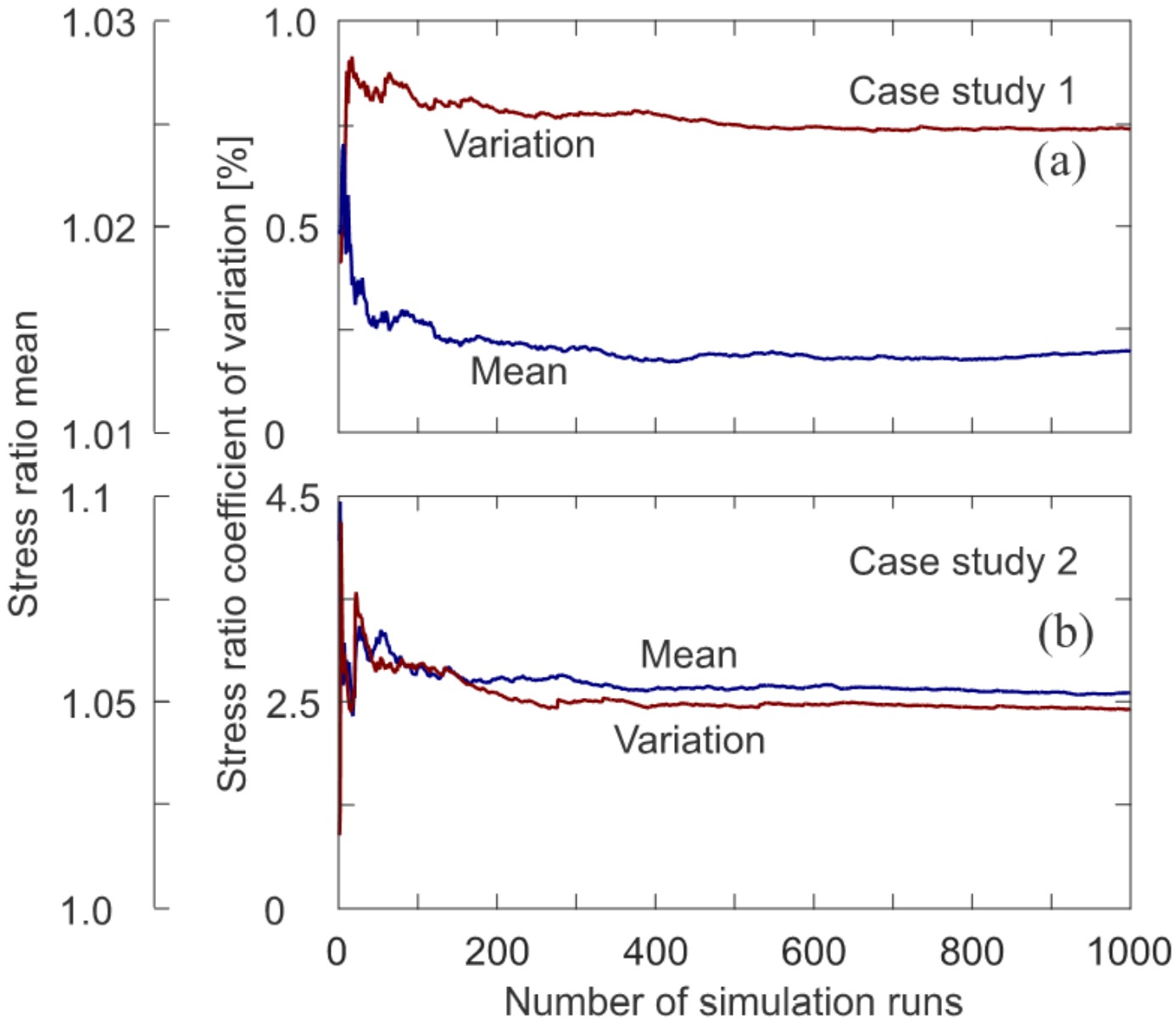

Figure 13

Convergence test for the stress ratio mean and coefficient of variation for case studies (a) 1 and (b) 2

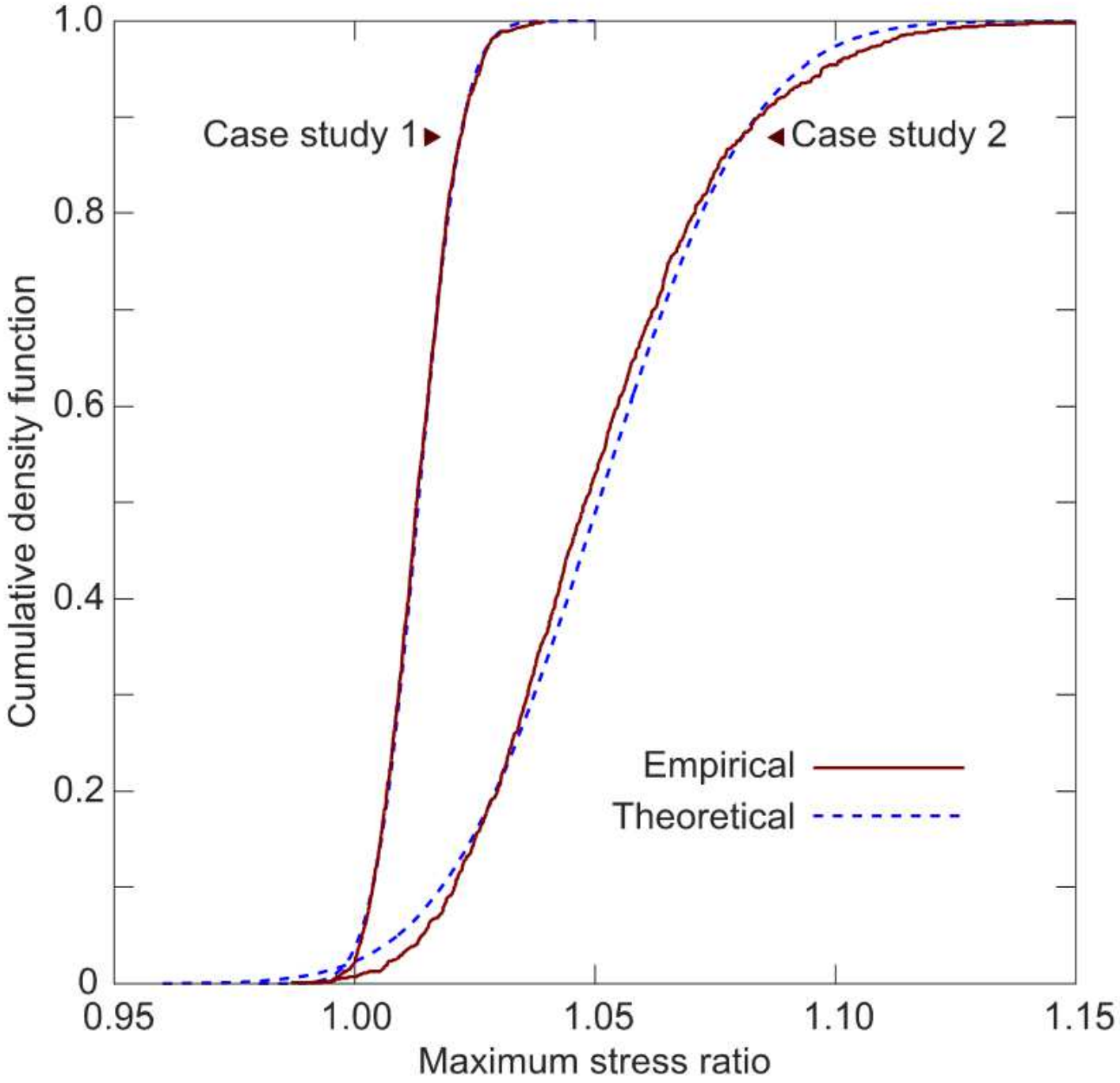

Figure 14

Cumulative density function of the maximum tensile stress ratio for case studies 1 and 2

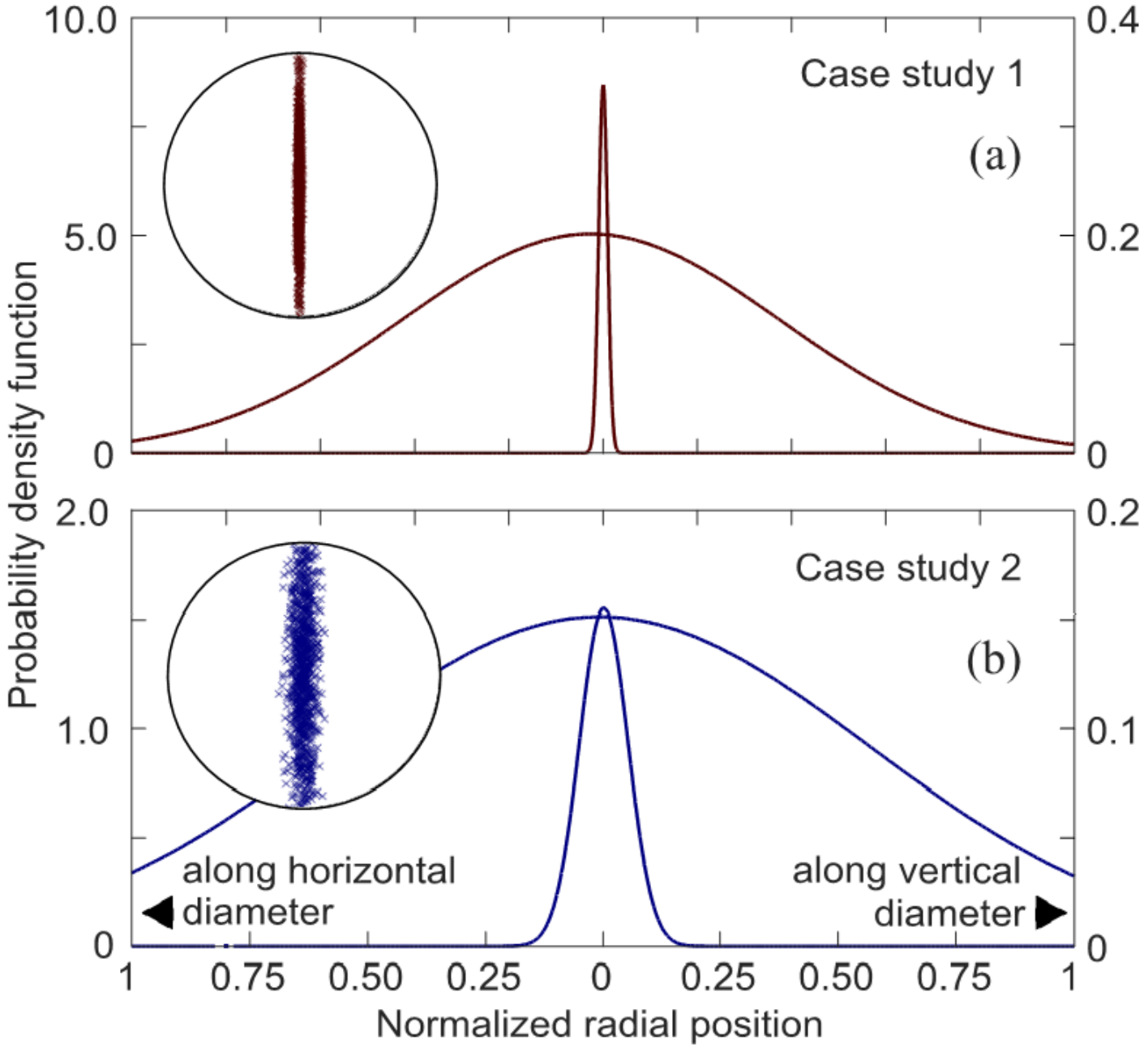

Figure 15

Statistical distributions for the location of the predicted maximum tensile stresses for case studies (a) 1 and (b) 2